

Lanthanide-Doped CaS and SrS Luminescent Nanocrystals: A Single-Source Precursor Approach for Doping

Yiming Zhao,^{†,||} Freddy T. Rabouw,[†] Tim van Puffelen,[†] Cornelis A. van Walree,^{†,‡} Daniel R. Gamelin,[§] Celso de Mello Donegá,[†] and Andries Meijerink^{*,†}

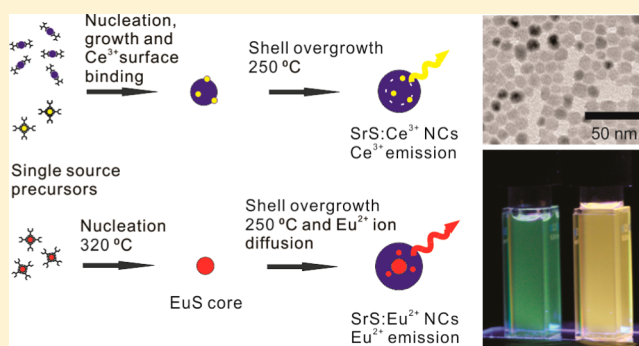
[†]Condensed Matter and Interfaces, Debye Institute for Nanomaterials Science, Utrecht University, Princetonplein 5, 3584 CC Utrecht, The Netherlands

[‡]School of Chemical and Physical Sciences, Flinders University, GPO Box 2100, Adelaide 5001, Australia

[§]Department of Chemistry, University of Washington, Seattle, Washington 98195-1700, United States

Supporting Information

ABSTRACT: The incorporation of dopants with optical or magnetic functionalities into colloidal nanocrystals (NCs) has been a longstanding challenge for nanomaterial research. A deeper understanding of the doping kinetics will aid a better control of the doping process. In particular, alkaline-earth sulfides are an important class of host materials for a range of luminescent dopants, including transition-metal and lanthanide ions. Their nanocrystalline analogues have many potential applications. However, the lack of synthetic methodologies hampers their development. Here we introduce a single-source precursor approach that successfully leads to Ce³⁺- and Eu²⁺-doped CaS and SrS luminescent NCs with diameters of ~10 nm and with luminescent properties similar to those of the bulk analogues. The characteristic absorption and luminescence of Ce³⁺ and Eu²⁺ depend on the local coordination and are applied to probe dopant ion internalization. We demonstrate that controlling the reactivity of the precursors is crucial for achieving effective doping. By designing the chemical structure of the dopant precursor to vary the reactivity relative to that of the host precursor, the doping efficiency can be controlled. In addition, we have applied a growth doping strategy to further improve internalization of the dopants. Finally, we demonstrate nucleation doping as an alternative method to achieve lanthanide NC doping for dopant and host precursors with strongly different reactivities. The single-source precursor approaches proposed here allow for a flexible design of synthesis strategies and have the potential to be widely applicable to the doping of colloidal chalcogenide NCs with transition-metal and lanthanide dopant ions.



INTRODUCTION

Doping impurities into nanocrystals (NCs) enables the introduction and tuning of optical, electrical, and magnetic properties.^{1–3} Growing interest in the development of new types of doped colloidal NCs is motivated by both fundamental science and potential applications. Successful NC doping requires an understanding of the doping process and the development of new doping strategies.

Previous efforts have mainly focused on two major classes of doped NCs: transition-metal-doped chalcogenide semiconductor II^B–VI NCs (e.g. CdSe,^{4,5} ZnSe,⁶ and ZnS⁷) and lanthanide-doped wide band gap insulator NCs (so far limited mainly to fluorides, phosphates, and oxides).^{2,8,9} In these wide band gap nanocrystals, lanthanides are in the trivalent state and are characterized by weak and narrow line absorption due to 4f–4f transitions, while the strong 4f–5d transitions are situated in the UV. For many applications, however, strong and broad band absorption and emission in the visible spectral region are required. A largely unexplored class of nanocrystal-

line host materials is the alkaline-earth sulfide II^A–VI NCs, e.g. CaS and SrS. As bulk materials they are well-known hosts for a variety of luminescent dopant ions, including Mn²⁺, Cu⁺, Ce³⁺, and Eu²⁺.¹⁰ The high luminescence quantum efficiencies, saturated emission colors, and high thermal stability of these materials make them interesting for a number of applications, including phosphors for color conversion in LED-based lighting.^{10,11} In addition, CaS:Ce³⁺, Sm³⁺ and CaS:Eu²⁺, Sm³⁺ are well-known afterglow (or persistent luminescence) materials.^{12,13} Their colloidal NCs are excellent candidates of nontoxic afterglow nanolabels for background-free biomedical imaging.¹⁴ In addition, lanthanide-doped alkaline-earth sulfide NCs may be applied for spectral conversion in luminescent solar concentrators.^{15,16}

The incorporation of dopants into colloidal NCs is, however, not always straightforward and is often the limiting factor in the

Received: July 28, 2014

Published: November 4, 2014

development of new doped NCs.^{1,17,18} Previously reported synthetic protocols for doped NCs of II^A–VI materials have relied on coprecipitation or hydrothermal methodologies,¹⁹ which yielded relatively large particles (tens to hundreds of nanometers), with ill-defined shapes and large size distributions.²⁰ The lack of synthetic methodologies for well-defined and monodisperse doped II^A–VI NCs has greatly hampered the development of this class of materials.

Recently there has been remarkable progress in the development of new doping strategies, especially for II^B–VI and IV–VI NCs. Single-source precursor decomposition, cation exchange,⁵ attachment followed by shell overgrowth (growth doping),²¹ diffusion doping,²² and nucleation doping have been successful in realizing host–dopant combinations that were not feasible through traditional methods. The use of single-source precursors (SSPs) was first developed for the synthesis of II^B–VI semiconductor NCs²³ and transition-metal sulfide NCs^{24–26} and has later been shown to have great potential for NC doping.^{18,27} Most previous reports have focused on the doping of transition metals,^{27–29} while very few examples have applied SSPs to lanthanide doping.¹⁸ The incorporation of lanthanide ions in II–VI NCs has been a challenge due to differences in preferred anion coordination, size, and charge between lanthanide dopants and the divalent host cations for which they substitute.^{17,21,30,31}

Here we report a SSP approach for successful doping of Ce³⁺ and Eu²⁺ in monodisperse ~10 nm colloidal SrS and CaS NCs. The optical properties of these dopant ions, which strongly depend on the local chemical environment, are used to probe and evaluate the efficiency of incorporation. For both Ce³⁺ and Eu²⁺ efficient d–f emission has been reported in bulk CaS and SrS. The spectra are characteristic for Eu²⁺ and Ce³⁺ in CaS or SrS. In other host materials the 4f¹ → 5d¹ transition on Ce³⁺ is typically located in the UV/blue spectral region. However, due to the high covalency (S²⁻ ligands) and large octahedral crystal field splitting, the lowest 5d state is shifted to low energy in CaS and SrS and is situated in the yellow-green spectral region. Similarly, for Eu²⁺, typically blue-green emission is observed but the same effects (covalency, crystal field) shift the Eu²⁺ emission to the orange-red spectral region in CaS and SrS.¹⁰ Due to the high sensitivity of the f–d luminescence spectra to the local environment, the observation of luminescence spectra that are typical for Ce³⁺ or Eu²⁺ in bulk CaS or SrS provides strong evidence that Ce³⁺ or Eu²⁺ is incorporated on the octahedral site inside the CaS or SrS nanocrystals. For Eu²⁺ or Ce³⁺ in solution or at the surface the coordination will be different and the emission is situated at shorter wavelengths. This makes luminescence spectroscopy a very sensitive tool for probing the incorporation of these lanthanide ions into chalcogenide nanocrystals. In addition, the strong, broad 4f–5d absorption and emission bands in the visible spectral region give Eu²⁺- and Ce³⁺-doped CaS and SrS nanocrystals unique optical properties for applications such as spectral conversion for solar cells and as biolabels.

To establish the kinetic and chemical conditions that enable effective dopant incorporation, a crucial factor is the balance between the reactivities of host and dopant precursors.¹⁸ To achieve this balance, the ligand–metal bond strength can be tuned by choosing the appropriate coordinating ligand.³² For SSPs the reactivity, measured as the decomposition temperature (T_D), is strongly related to the chemical structure.³³ In this report, we have systematically studied the influence of the reactivity of SSPs on the doping level in the NCs. We

demonstrate that, by changing the SSP structure, hence tuning their reactivities, the doping efficiency can be improved and controlled. Moreover, we demonstrate the flexibility of synthesis methods based on SSPs through combination with other strategies, including growth doping^{34,29} and nucleation doping,^{35,36} to synthesize monodisperse luminescent lanthanide-doped CaS and SrS nanocrystals.

RESULTS AND DISCUSSION

Growth Doping for SrS:Ce³⁺, CaS:Ce³⁺, and SrS:Eu²⁺ NCs. A single-source precursor method was recently developed for synthesis of monodisperse ~10 nm SrS and CaS NCs, through thermal decomposition of strontium diisopropylthiocarbamate (Sr(DPTC)₂) and calcium diisopropylthiocarbamate (Ca(DPTC)₂) in oleylamine at 250 °C.³⁷ In order to incorporate Ce³⁺ or Eu²⁺ dopants in CaS or SrS NCs, a straightforward method is to simultaneously decompose the SSPs of both the host material and the dopant together through a hot-injection strategy. In Figure 1 the method is schematically

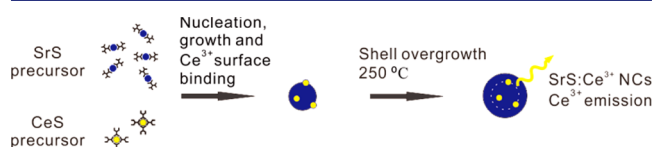
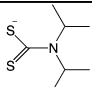
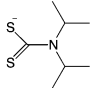
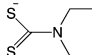
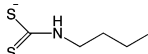
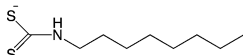
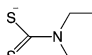
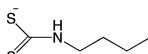
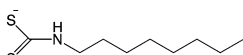
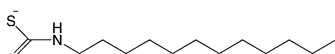


Figure 1. Schematic illustration of the synthesis of SrS:Ce³⁺ NCs using single-source precursors and a growth doping strategy.

depicted for SrS:Ce³⁺. In Table 1 the chemical structures of the various SSPs used in this report are collected. Coinjection of Sr(DPTC)₂ and cerium diethylthiocarbamate (Ce(DDTC)₄, 5 mol % with respect to Sr) in oleylamine at 250 °C results in the formation of 8–10 nm NCs (Figure 2a). The solution is slightly yellow, indicating incorporation of Ce³⁺ (vide infra). After recapping the NCs with oleic acid and tetradecylphosphonic acid and washing with methanol, the NCs were redispersed in toluene or hexane (see the Experimental Section for details). We observed through TEM that the sizes of the particles collected from the reaction solution immediately after the injection of precursors did not significantly differ from those collected after several minutes (data not shown). This implies that the NCs nucleate and reach their final size within a few seconds in oleylamine at 250 °C. Therefore, the size of the particles is mainly controlled by adjusting the concentration of precursors, with higher concentrations leading to larger NC sizes (see TEM images in the Supporting Information, Figure S1). The size of the NCs obtained is similar to the size reported for undoped SrS NCs synthesized for similar SSP concentrations.³⁷ The coordinating solvent, oleylamine, assists the decomposition of dithiocarbamate salts by lowering the decomposition temperature.²⁵ This mechanism has been described in detail recently.³⁸

To improve the incorporation of Ce³⁺ ions in the SrS NCs, the shell overgrowth method was applied. Previously, in many doped NC systems (e.g., CdS:Co²⁺,³⁴ ZnSe:Mn²⁺,³⁵ and CdS/ZnS:Mn²⁺),³⁹ epitaxial growth of additional layers of host material was used to increase the doping level, by internalizing surface-bound dopant ions. In a similar way, we grew a SrS shell over the SrS:Ce³⁺ NCs formed after the coinjection, by slowly adding Sr(DPTC)₂ precursor solution to the reaction mixture at 250 °C (as schematically illustrated in Figure 1). Figure 2a shows that the SrS:Ce³⁺ NCs formed after the coinjection have

Table 1. Decomposition Temperatures and Structures of Single-Source Precursors in Oleylamine

Precursors	Structure of ligand	Decomp. Temp. (°C) ^a	Phenomenon used to indicate decomposition
Ca(DPTC) ₂		140	Generation of H ₂ S gas, formation of CaS
Sr(DPTC) ₂		140	Generation of H ₂ S gas, formation of SrS
Ce(DDTC) ₄		150	Dark brown solution, formation of CeS
Ce(BDTC) ₄		135	Dark brown solution, formation of CeS
Ce(ODTC) ₄		115	Dark brown solution, formation of CeS
Eu(DDTC) ₄		260	Purple solution, formation of EuS
Eu(BDTC) ₄		131	Purple solution, formation of EuS
Eu(ODTC) ₄		125	Purple solution, formation of EuS
Eu(DoDTC) ₄		115	Purple solution, formation of EuS

^aThe decomposition of the precursor in oleylamine takes place over a temperature range of typically 6–8 °C at a heating rate of 5 °C/min. For simplicity, the T_D value presented here is roughly the middle point of the decomposition range.

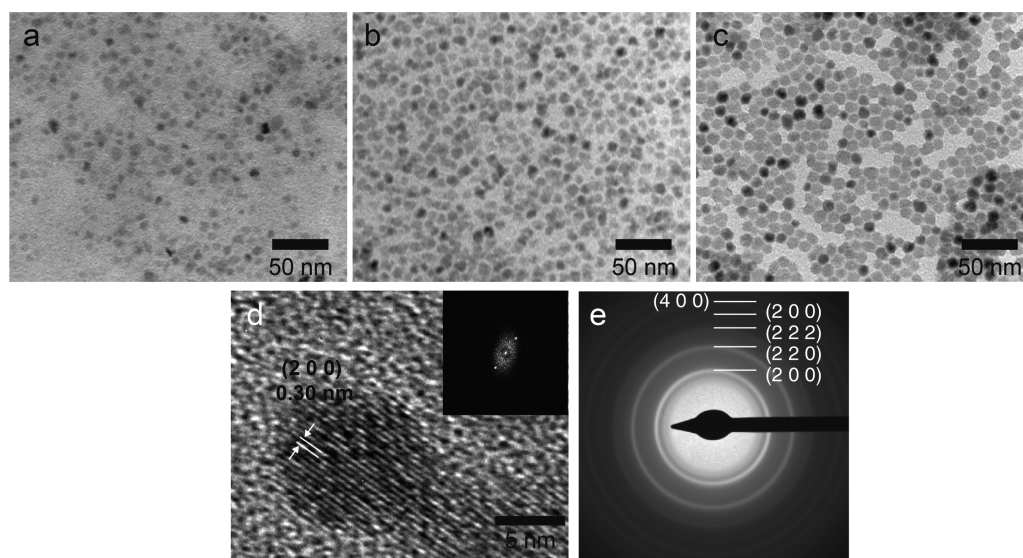


Figure 2. TEM images of SrS:Ce³⁺ NCs obtained through the growth doping method: (a) after coinjection of lattice and dopant precursors; (b) after shell overgrowth; (c) after annealing at 270 °C for 1 h. (d) HR-TEM image of a single SrS:Ce³⁺ NC. The inset shows the fast Fourier transform (FFT) of the image, which is used to determine the spacing of (200) planes. (e) Electron diffraction pattern of an ensemble of SrS:Ce³⁺ nanocrystals and the assignments of diffraction rings.

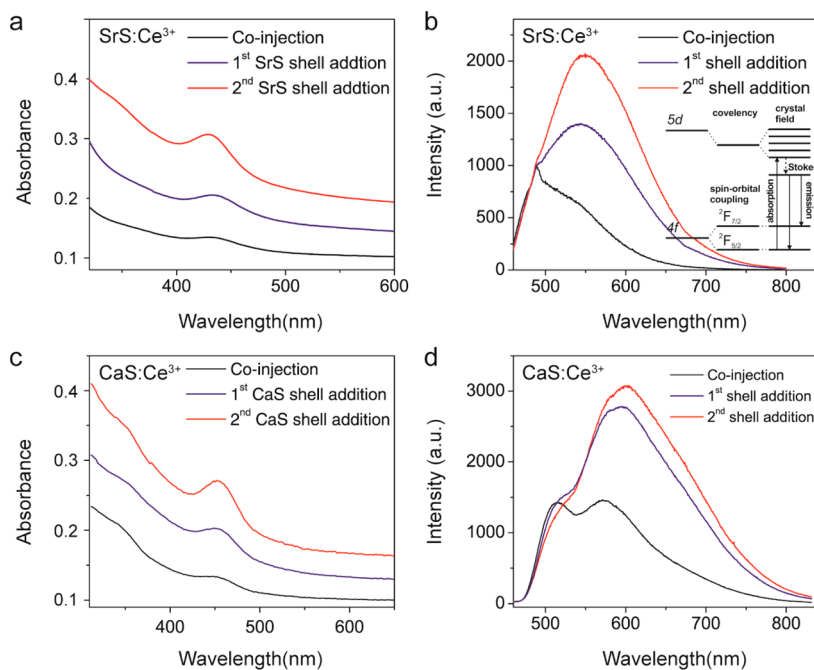


Figure 3. (a) Absorption and (b) emission spectra of SrS:Ce³⁺ NCs samples (for 430 nm excitation) obtained during the synthesis through the growth doping method. The small peak at ~490 nm is due to Raman scattering, which is observable when emission peak is weak. The inset shows the energy levels of Ce³⁺ ions (4f¹) in a host lattice. The energy of the f–d transition is influenced by the nephelauxetic effect (through covalency), crystal field splitting, and phonon coupling. (c) Absorption and (d) emission spectra of CaS:Ce³⁺ NCs through the growth doping method.

irregular shapes and diameters around 8–10 nm with a rather large polydispersity (>30%). After the addition of the SrS shell precursors, the size of the NCs increased to 10–12 nm (Figure 2b), confirming the growth of a SrS shell around the pre-existing SrS:Ce³⁺ NCs. After annealing at 270 °C for 1 h, the NCs were more spherical and the size distribution was narrower (<10%, Figure 2c). High-resolution TEM images (Figure 2d) confirm the single-crystalline nature of the SrS:Ce³⁺ NCs, since no grain boundaries are observed within individual NCs. Electron diffraction patterns are consistent with the rock salt structure of SrS (Figure 2e). XRD analysis confirms the formation of SrS NCs, while there is no evidence for the formation of Ce₂S₃ nanocrystals (see XRD patterns in the Supporting Information, Figure S2).

To follow the incorporation of Ce³⁺ into the SrS NCs, optical absorption spectra were recorded. Figure 3a shows the absorption spectrum of the SrS:Ce³⁺ NCs obtained after the coinjection of Sr and Ce precursors followed by SrS shell growth. The broad absorption band at 430 nm is assigned to the 4f¹ → 5d¹ transition of Ce³⁺ ions in SrS, and its spectral position is in good agreement with the values reported for bulk SrS:Ce³⁺.⁴⁰ In addition, the emission spectrum of the SrS:Ce³⁺ NCs obtained after the coinjection (Figure 3b) is consistent with emission spectra previously reported for bulk SrS:Ce³⁺.^{40,41} In the Supporting Information, Figure S4, the luminescence spectra for Ce³⁺ in bulk SrS are included for comparison. The spectra show a broad emission band centered at ~480 nm with a shoulder at ~540 nm. An emission spectrum showing two bands split by about 2000 cm⁻¹ is typical for Ce³⁺ d–f emission, due to the 2000 cm⁻¹ spin–orbit splitting of the ²F ground state into ²F_{5/2} and ²F_{7/2} states. A similar doping strategy was applied for the synthesis of CaS:Ce³⁺ NCs (see the TEM image in the Supporting Information, Figure S3, and XRD pattern in the Supporting Information, Figure S2). After the coinjection of Ca and Ce

SSPs, a weak absorption peak at 450 nm and a corresponding double-emission peak at 514 and 572 nm appeared (Figure 3c,d), consistent with the optical spectra reported for Ce³⁺ in bulk CaS (see also the Supporting Information, Figure S4).^{40,42} The typical double peak structure is only clearly observed before shell overgrowth. After shell overgrowth the Ce³⁺ concentration in the NCs increases and in the transparent solution reabsorption effects distort the shape of the emission spectra due to the overlap between the absorption and emission spectrum, as will be discussed in the next section. The yellow coloration of the reaction mixture is indicative of incorporation of Ce³⁺ in CaS and SrS. It arises from the Ce³⁺ f–d absorption band in the blue-green spectral region in these host lattices. More quantitative information is obtained from luminescence and absorption spectra for the f–d transition on Ce³⁺. The spectra in Figure 3 provide direct proof of the successful incorporation of Ce³⁺ into SrS and CaS NCs. Ce³⁺ absorption and emission spectra are sensitive to the local coordination, as discussed in the Introduction. Emission in the yellow or orange spectral region is only possible in highly covalent host lattices and/or in the case of a strong crystal field splitting (Figure 3b inset) as in SrS and CaS. The shift of the d–f absorption and emission to 20 nm longer wavelengths for Ce³⁺ in CaS in comparison to SrS is due to the larger crystal field splitting for the 5d orbitals for Ce³⁺ on the smaller Ca²⁺ site. The larger crystal field splitting shifts the lowest t_{2g} state to lower energies. Note that the emission spectrum of Ce³⁺ in the SrS or CaS NCs is the same as that for Ce³⁺ in the bulk analogue, since the transitions are localized on the Ce³⁺ ion and the coordinating anions (S²⁻). Hence, in contrast to the undoped semiconductor NCs, where quantum confinement effects for the delocalized exciton result in size-dependent emission colors, the emission spectra of SrS:Ce³⁺ and CaS:Ce³⁺ do not depend on the crystal size. The observation of the characteristic absorption and emission for Ce³⁺ in an octahedral S²⁻ coordination in CaS or

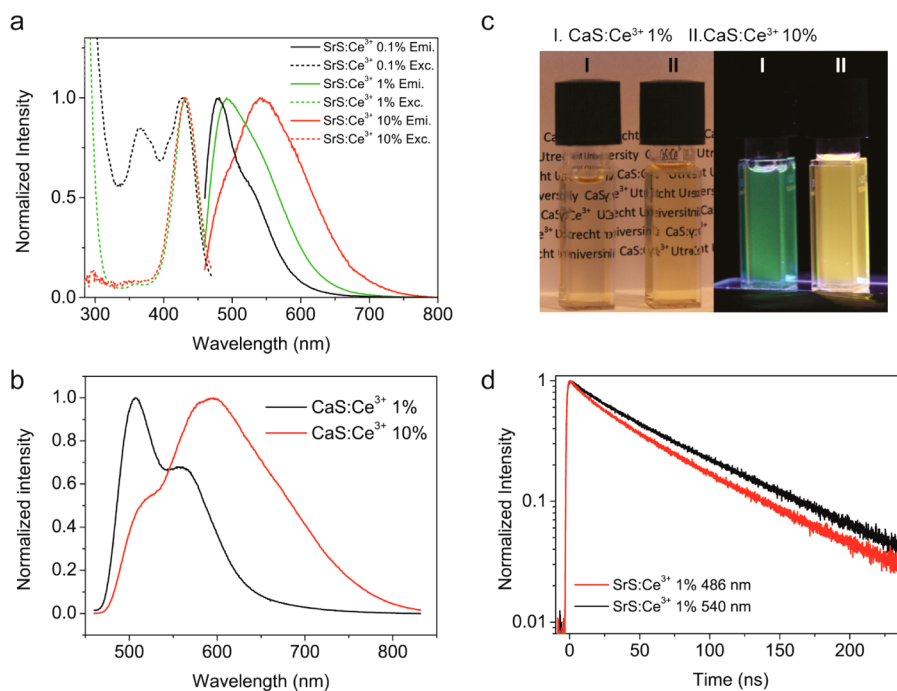


Figure 4. (a) Emission (solid lines) and excitation (dashed lines) spectra of SrS:Ce³⁺ NCs with 0.1%, 1%, and 10% Ce³⁺ in the reaction mixture. All emission spectra are recorded with excitation at 430 nm. Excitation spectra are recorded at peak emission wavelengths. The excitation peak at 430 nm is direct excitation of the Ce³⁺ ions, and the peak at 375 nm may be due to defect states in the lattice. (b) Emission spectra of CaS:Ce³⁺ with 1% and 10% of Ce precursor content, excited at 450 nm. (c) Colloidal suspension of CaS:Ce³⁺ 1% and 10% NCs in toluene under ambient light (left) and UV irradiation (right). (d) Luminescence decay curves of SrS:Ce³⁺ NCs emission at 486 and 540 nm, excited with a picosecond UV diode at 277 nm.

SrS can be utilized to distinguish incorporated Ce³⁺ from surface-bound Ce³⁺. Ce³⁺ on the surface has a different local coordination, resulting in absorption and emission spectra that differ from those of fully internalized Ce³⁺. Hence, the similarity of the absorption and emission spectra in Figure 3a to those observed for Ce³⁺ in bulk SrS and CaS (see Figure S4) confirms that Ce³⁺ has been successfully incorporated. The ability to assign the luminescence spectra of Ce³⁺ specifically to internally doped ions is important, since it is a notorious problem to distinguish between dopant ions at the surface and dopant ions incorporated in a NC.^{1,3,18}

The results clearly show that Ce³⁺ doping in SrS and CaS can already be achieved through the coinjection of lattice and dopant SSPs. The weak Ce³⁺ absorption peak and low emission intensities suggest that a substantial fraction of the Ce³⁺ ions is not incorporated. In the emission spectrum recorded for the sample immediately after coinjection, the Ce³⁺ emission intensity is weak, especially for SrS, and a Raman peak is observed at 490 nm, while there may also be a weak blue background emission from defect states in the SrS lattice (Figure 3b). The 490 nm Raman peak is due to a ~ 2900 cm⁻¹ C–H vibration in solution and can be observed in weakly luminescent samples. Evidence for the assignment to a Raman peak is the 2900 cm⁻¹ lower energy with respect to the excitation wavelength (430 nm) and the shift of the peak along with the excitation wavelength. During the addition of shell precursors the reaction solution darkens from light to deep yellow. This color change is clearly reflected in the absorption spectra from the samples taken at two time points during the shell growth (Figure 3a,c), since the Ce³⁺ absorption strength at 430 nm increases after addition of more host precursor. Correspondingly, the intensity of the Ce³⁺ emission is strongly

enhanced (Figure 3b). The intensity of the emission peak at 540 nm ($5d \rightarrow 2F_{7/2}$) increases more than the peak at 480 nm ($5d \rightarrow 2F_{5/2}$) and becomes dominant. These observations indicate that the SrS shell growth has successfully internalized more Ce³⁺ ions in the SrS NCs while also some unreacted Ce³⁺ in the reaction mixture may be incorporated during the shell overgrowth. Similar to the case for SrS:Ce³⁺ NCs discussed above, also for CaS:Ce³⁺, the intensity of the Ce³⁺ absorption and emission bands increases upon growth of CaS shells over the CaS:Ce³⁺ NCs, confirming the internalization of Ce³⁺ ions in the CaS NCs. The red shift of the emission peak upon increasing Ce³⁺ concentration is due to reabsorption effects in the nanoparticles and will be discussed in more detail in the next section.

Following the successful Ce³⁺ doping strategy, a similar synthesis method was applied to dope Eu²⁺ in SrS and CaS NCs by using europium diethyldithiocarbamate (Eu(DDTC)₄) as the dopant precursor (see the Experimental Section for details). Absorption and emission spectra recorded for the NCs did not show the characteristic absorption or emission of Eu²⁺ in SrS (see the Supporting Information, Figure S4, for the bulk spectra), indicating that the doping was not successful. Only when the reaction temperature was increased to temperatures as high as 340 °C was weak Eu²⁺ emission observed in some syntheses, but with very poor reproducibility. To understand the difference in doping kinetics for Eu²⁺ and Ce³⁺ in SrS and CaS, decomposition temperatures in oleylamine, T_D , were determined for the various single-source precursors. The T_D value of Eu(DDTC)₄ is over 260 °C (consistent with that reported in the literature⁵⁰), while the T_D value of Ce(DDTC)₄ is around 150 °C, which is much lower and also closer to Sr(DPTC)₂ or Ca(DPTC)₂ (both around 140 °C; see Table

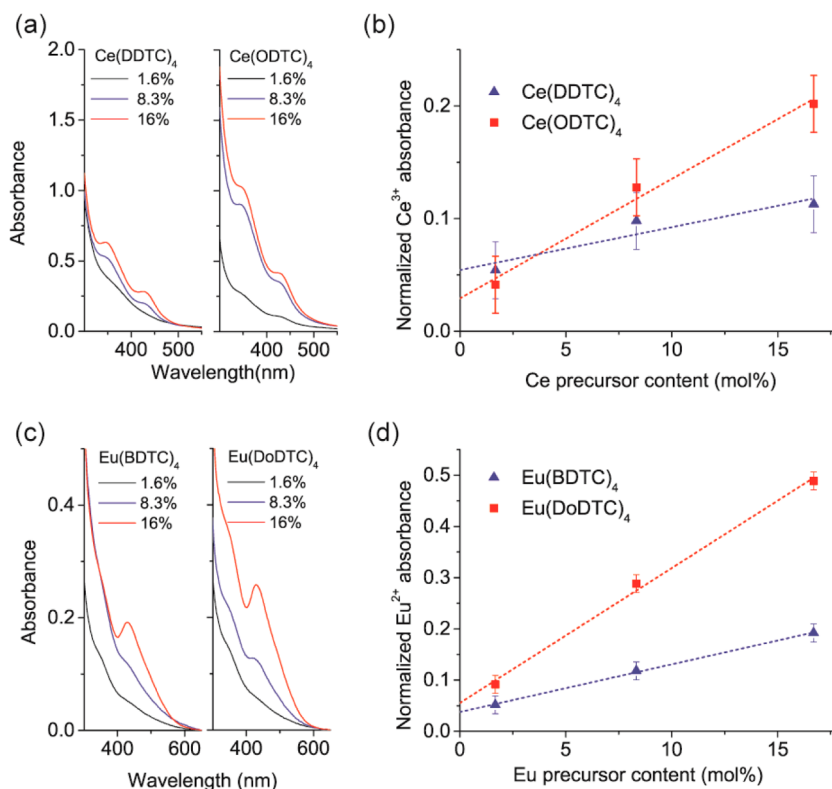


Figure 5. (a) Absorption spectra of SrS:Ce³⁺ NCs synthesized by codecomposing Sr(DPTC)₂ and Ce(DDTC)₄ (left)/Ce(ODTC)₄ (right), on increasing the concentration of dopant precursors. (b) Absorbance of Ce³⁺ in SrS:Ce³⁺ (normalized to SrS absorbance at 300 nm) plotted against the relative concentrations of Ce precursors. (c) Absorption spectra of SrS:Ce³⁺ NCs synthesized by codecomposing Sr(DPTC)₂ and Eu(BDTC)₄ (left)/Eu(DoDTC)₄ (right), on increasing the concentration of Eu dopant precursors. (d) Absorbance of Eu²⁺ in SrS:Eu²⁺ (normalized to SrS absorbance at 300 nm) plotted against the relative concentrations of Eu precursors. In (b) and (d) the dotted lines are linear fits. The nonzero intersection with the y axis is attributed to scattering by the samples. The scattering also contributes to the error in the measured absorbance.

1). We hypothesize that T_D (or the decomposition rates at the reaction temperature) values of dopant and lattice precursors are crucial factors for successful doping via the SSP method. For a high doping efficiency, dopant SSPs with high reactivity, reflected in a similar or lower T_D value in comparison to that of the host precursor, are required.

Luminescence Properties and the Effect of Ce³⁺ Concentration. To investigate the dependence of the optical properties on the doping concentration, a series of SrS:Ce³⁺ and CaS:Ce³⁺ NCs was synthesized by the growth doping method for different ratios of Ce to Sr/Ca precursors. For low doping concentrations the characteristic emission spectra for Ce³⁺ and Eu²⁺ in CaS and SrS are observed, providing strong evidence for the incorporation of these ions in the CaS and SrS nanocrystals. The emission spectra are observed to significantly red shift and broaden with increasing Ce³⁺ concentration in the reaction mixture for both SrS:Ce³⁺ and CaS:Ce³⁺ NCs (Figure 4a,b). The effect of doping concentration on the emission spectrum is quite pronounced, leading to a change of luminescent color for CaS:Ce³⁺ NCs from green to yellow, when the Ce³⁺ concentration (in the reaction mixture) increases from 1 to 10 mol % (Figure 4c). The relative intensity of two emission bands (*viz.*, $5d(t_{2g}) \rightarrow 2F_{5/2}(4f)$ and $5d(t_{2g}) \rightarrow 2F_{7/2}(4f)$) changes dramatically. Similar concentration effects have been reported for bulk SrS:Ce³⁺ or CaS:Ce³⁺ phosphors and were ascribed to radiative (self-absorption) and nonradiative energy transfer from Ce³⁺ ions emitting at higher energy (donors) to slightly perturbed Ce³⁺ ions emitting at lower energies.^{43,44} Reabsorption of the short

wavelength emission is possible due to spectral overlap of the emission and absorption spectrum in the region of the short-wavelength emission (see also Figure S4 in the Supporting Information). Figure 4a also presents the excitation spectra of the SrS:Ce³⁺ NCs recorded at emission maxima. The peak at 430 nm is assigned to the direct excitation of the Ce³⁺ ions, and the continuous band ($\lambda < 320$ nm) is from the excitation on the SrS host lattice and the subsequent energy transfer to the activator Ce³⁺.

Luminescence decay measurements on SrS:Ce³⁺ NCs while the 486 and 540 nm emission peaks were monitored gave nearly single-exponential decay curves, with fitted lifetimes of 56 and 65 ns, respectively (Figure 4d). The nonexponential faster decay observed in the initial part for the 486 nm emission is explained by energy transfer to perturbed Ce³⁺ ions emitting at longer wavelengths. A comparison of the lifetimes with values reported for bulk SrS:Ce³⁺ (27–36 ns)^{41,45} show a slower decay of the Ce³⁺ emission in SrS nanocrystals. This can be ascribed to the lower density of optical states in NCs leading to slower radiative rates in comparison to bulk crystals, based on the theory of local-field effects in nanocrystals (see the Supporting Information for details).^{46,47} However, on the basis of the same theory, we estimate that the radiative lifetime of SrS:Ce³⁺ NCs dispersed in hexane should be 90–120 ns, about 1.5–2 times longer than the experimental lifetime. Hence, we calculate that the quantum efficiency of the emitting Ce³⁺ ions in our NCs is 50%–67%. In contrast, with an integrating sphere measurement we measured an ensemble quantum yield of 9%. This leads to the conclusion that, while the bright Ce³⁺ ions

have a quantum efficiency of as high as 50–67%, a considerable fraction (82–87%) of the ions is dark. This phenomenon, of an ensemble of luminescent species consisting of a bright fraction (with high quantum efficiency) and a dark fraction, is well-known for luminescent semiconductor nanocrystals.^{48,49} The fraction of dark Ce^{3+} ions is relatively large, probably because a single quenching site in a nanocrystal can quench several nearby Ce^{3+} centers. The presence of a single imperfection (e.g., a Ce^{3+} ion on a perturbed surface site, a Ce^{4+} ion, or a defect) may thus render a nanocrystal completely dark. For application of the luminescent nanocrystals a higher quantum yield is required. Additional shell growth (e.g., ZnS) or postsynthesis annealing are strategies for improving the optical properties.

Balancing the Reactivity of SSPs by Tuning Their Decomposition Temperature. Above it was shown that doping of Ce^{3+} into CaS and SrS NCs was successful through SSP decomposition, while for Eu^{2+} no successful incorporation in CaS or SrS could be achieved. As an explanation a high decomposition temperature (low reactivity) of the $\text{Eu}(\text{DDTC})_4$ precursor was suggested. To examine this hypothesis and to systematically investigate the relation between the SSP reactivity and the doping efficiency, a series of Ce and Eu precursors with varying T_D values were synthesized and were applied to the doping of SrS NCs (see Table 1 for the structures and the Supporting Information, Figure S5, for the corresponding IR spectra of different precursors). O'Brien et al. have reported that the T_D values of metal dithiocarbamate complexes are related to the structures of the ligands.⁵¹ Ligands with a monoalkyl group have lower T_D values in comparison to those with a dialkyl group, and the longer the chain length of alkyl groups, the lower the T_D value. Our findings here are consistent with these trends.

It is worth noting that, for NC doping through SSPs, the reaction temperature also plays a significant role, since it not only affects the reactivity of the SSPs but also influences other kinetic factors of the doping chemistry, including the surface and interior related processes (as discussed later).^{36,52} To simplify the discussion, in this section we fix the reaction temperature at 250 °C.

First, we investigated the effect of the decomposition temperature of the dopant SSP by synthesizing SrS: Ce^{3+} under identical conditions with two different SSPs: Ce-(DDTC)₄ ($T_D = 150$ °C) and cerium octyldithiocarbamate (Ce(ODTC)₄; $T_D = 115$ °C). After coinjection of the host and dopant precursor (with 1.6, 8.3, and 16 mol % of dopant precursor) into oleylamine, the reaction proceeded for 3 min before samples were taken and washed. The total Ce concentration in the SrS: Ce^{3+} NCs (both lattice incorporated or surface attached) was determined by ICP-AES (see the Supporting Information, Table S1 and Figure S6). An approximately linear relation was found between the total Ce concentration in the NCs and the Ce precursor concentration. The steeper slope observed for the synthesis using Ce(ODTC)₄ implies more efficient decomposition of precursors with lower T_D . To quantify the real amount of Ce^{3+} incorporated inside the SrS lattice, the characteristic Ce^{3+} f–d absorption was measured. Figure 5a shows the absorption spectra of SrS: Ce^{3+} NCs obtained using Ce(DDTC)₄ (Figure 5a, left) and Ce(ODTC)₄ (Figure 5a, right) for varying Ce precursor concentrations. The Ce^{3+} incorporation ratios were estimated from the absorbance of Ce^{3+} ions in SrS (at 430 nm) normalized to the interband absorbance of the SrS host

material (at 300 nm). An absorption shoulder around 350 nm is also observed and is assigned to Ce^{3+} ions at the NC surface. The only partial S^{2-} coordination can explain the higher energy position of the 5d state for surface-bound Ce^{3+} in comparison to full S^{2-} coordination. Although scattering introduces uncertainties in the measured absorption intensity and causes the nonzero interception of the linear fit in Figure 5b, the results show that, for both precursors, increasing the dopant precursor content leads to a stronger absorption and thus a higher concentration of incorporated Ce^{3+} ions. Moreover, the steeper slope of the linear trend reveals that more efficient dopant incorporation is obtained for Ce(ODTC)₄, the precursor with a lower T_D value.

To investigate the Eu SSPs for doping efficiency in SrS, europium butyldithiocarbamate ($\text{Eu}(\text{BDTC})_4$, $T_D = 131$ °C) and europium dodecyldithiocarbamate ($\text{Eu}(\text{DoDTC})_4$, $T_D = 115$ °C) were compared. Figure 5c shows the absorption spectra obtained for the resulting SrS: Eu^{2+} nanoparticles. The broad absorption band around 435 nm is ascribed to the characteristic $4f^7 \rightarrow 4f^6 5d^1(t_{2g})$ transition of Eu^{2+} in SrS, which is well-known from bulk SrS: Eu^{2+} phosphors.^{40,53} The observation of these absorption bands indicates the successful incorporation of Eu^{2+} ions in SrS NCs by using $\text{Eu}(\text{BDTC})_4$ and $\text{Eu}(\text{DoDTC})_4$, and XRD analysis confirms the formation of SrS nanocrystals (see XRD patterns in the Supporting Information, Figure S2). In Figure 5d the Eu incorporation efficiency, again quantified as the intensity ratio between the Eu^{2+} absorption (at 445 nm) and the SrS interband absorption (at 300 nm), is plotted against the relative dopant precursor concentration in the reaction mixture. Similar to the results for Ce^{3+} doping, the slope is steeper for the SSP with lower T_D (here, $\text{Eu}(\text{DoDTC})_4$). These results on Eu doping confirm that using a dopant SSP with a higher reactivity leads to a higher doping efficiency.

To understand the results, a simple kinetic model can be applied. As depicted in Figure 6, after injection, the dopant and

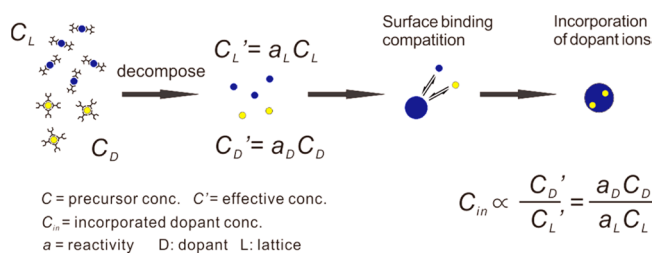


Figure 6. Schematic illustration of the doping mechanism for the single-source precursor method and the kinetic model proposed.

lattice SSPs (with concentrations C_D and C_L , respectively) start to decompose into reactive species. In the reaction solution, the effective concentrations (C'_D and C'_L) of the reactive species are related to the reactivity of the dopant and lattice SSPs, a_D and a_L , respectively. During the growth of the NC, dopant and lattice reactive species compete to bind on the NC surface. Therefore, despite the possible difference in their surface binding energies (or their corresponding lattice solubility products), the final dopant incorporation, C_{in} , is affected not only by the ratio of precursor concentrations (C_D/C_L) but also by the ratio of SSP reactivities, a_D . The concentration of dopant incorporated, C_{in} , is then

$$C_{in} \propto \frac{C_D'}{C_L'} = \frac{a_D C_D}{a_L C_L} \quad (1)$$

This equation explains why in Figure 5b,d the dopant SSPs with lower T_D values have a steeper slope in comparison to the less reactive dopant SSPs and suggests that, by adjusting the ligand structure of SSP, the doping efficiency can be improved. For a low-reactivity dopant SSP, a poor doping efficiency is expected. This explains that using $\text{Eu}(\text{DDTC})_4$, as mentioned at the beginning of this section, does not lead to Eu^{2+} doping because of its very high decomposition temperature of 260 °C. Note that in this model it is assumed the reaction does not proceed to complete incorporation of all precursors in nanocrystals, as in that case the dopant concentration will always be the same as the initially added concentration. For various doping methods it is generally observed that the dopant concentration in NCs is lower than that in the reaction mixture, indicating a preference for incorporation of the host cations.^{7,27}

The use of more reactive Eu SSPs with monoalkyl groups ($\text{Eu}(\text{ODTC})_4$ or $\text{Eu}(\text{DoDTC})_4$) leads to successful doping, but simple coinjection of the Eu and lattice SSPs results in low doping levels, just as observed for Ce^{3+} . The growth doping method enhances the Eu incorporation. Upon shell growth, a gradual change of the solution color was observed from light orange to red. Absorption spectra reveal that the Eu^{2+} band gradually increases in intensity and red shifts as the shell grows (Figure 7a). The increase in intensity of this absorption is a good indicator for the incorporation of Eu^{2+} into the NC. Accordingly, the characteristic Eu^{2+} emission in SrS at 610 nm also gradually increases in intensity and red shifts with additional SrS shell growth (Figure 7b). The excitation

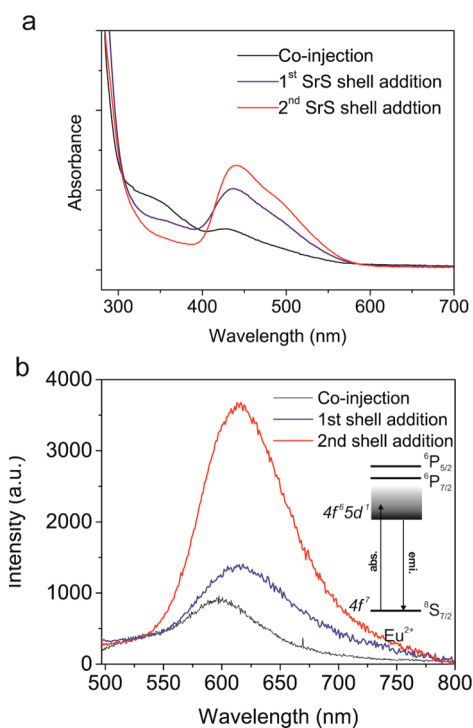


Figure 7. (a) Absorption and (b) emission spectra of SrS:Eu²⁺ NCs obtained during synthesis by the growth doping method. The inset shows the energy levels of Eu²⁺ ions (4f⁷). The energy of the 4f⁶5d¹ emission is influenced by the same effects as the Ce³⁺ d–f emission. Depending on the host, the lowest 4f⁶5d level can be below or above the ⁶P_{7/2} level of the 4f⁷ configuration.

spectrum and luminescence decay curve of SrS:Eu²⁺ NCs are shown in the Supporting Information, Figure S7. It should be noted that Eu²⁺ emission could only be observed when the shell growth was carried out at relatively low temperatures (200 °C). Shell growth at higher temperatures (e.g., 250 °C, which was successful for SrS:Ce³⁺ doping), does lead to incorporation of Eu²⁺, as evidenced by the increase of Eu²⁺ absorption (data not shown), but the Eu²⁺ emission is still weak or absent. This observation can be explained by considering that, at higher shell growth temperatures, Eu²⁺ ions will be able to diffuse into and through the SrS shell, thereby reaching the surface vicinity, where they will suffer from quenching by surface defect states. These results are summarized schematically in Figure 8.

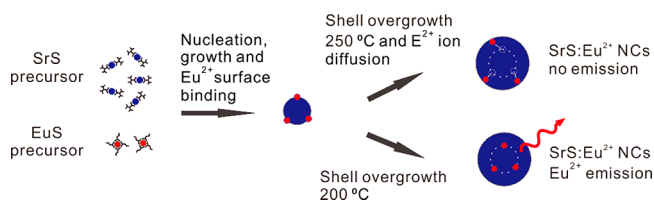


Figure 8. Schematic illustration of the synthesis of SrS:Eu²⁺ NCs using the single-source precursor method and the growth doping strategy. Eu²⁺ emission is observed only when the shell growth temperature is lower than 250 °C.

The results presented above demonstrate successful incorporation of lanthanide ions inside CaS and SrS NCs. For II^B–VI type NCs attempts to dope with lanthanides result in surface absorption rather than incorporation. The successful inclusion in CaS and SrS NCs can be understood from the similarity in ionic radii of the lanthanide dopants (1.17 Å for Eu²⁺ and 1.01 Å for Ce³⁺ in VI coordination)⁵⁴ and host cations (1.18 Å for Sr²⁺ and 1.00 Å for Ca²⁺ in VI coordination).⁵⁴ More importantly, in II^B–VI chalcogenide nanocrystals the host (zinc blende or wurtzite structure) offers only a IV-coordinated cation site. Lanthanide ions have a strong preference for VI coordination (or higher).⁵⁴ This hampers incorporation in II^B–VI type NCs and leads to lanthanide ions located on the surface. In the rock salt structure of II^A–VI chalcogenides the availability of a VI-coordinated cation site helps incorporation of lanthanide ions.

Nucleation Doping Method for SrS:Eu²⁺ NCs. The results discussed above demonstrate successful Eu²⁺ doping of SrS NCs and suggest that at sufficiently high temperatures Eu²⁺ is able to diffuse through the SrS lattice. This is not unexpected, since Eu²⁺ and Sr²⁺ have the same charge and very similar ionic radii (1.17 and 1.18 Å, respectively, in VI coordination).⁵⁴ On the basis of this observation, we applied an alternative doping method relying on dopant ion diffusion. The nucleation doping strategy was first introduced by Peng et al. for the synthesis of Mn²⁺-doped ZnSe nanoparticles.³⁵ Here we show that this approach, schematically depicted in Figure 9, can be successfully extended to lanthanide ion doped wide band gap NCs.

First, small (3–4 nm) EuS cores were synthesized through rapid decomposition of $\text{Eu}(\text{DDTC})_4$ in oleylamine at 320 °C. The formation of small EuS nuclei was confirmed by TEM imaging (Figure 10a) and optical absorption spectroscopy (Figure 11a). The EuS NCs have a characteristic absorption band centered at 504 nm, originating from the 4f⁷ → 4f⁶5d¹ (*t*_{2g}) transition of Eu²⁺.^{50,55} Note that we used the $\text{Eu}(\text{DDTC})_4$ precursor with high decomposition temperature for the

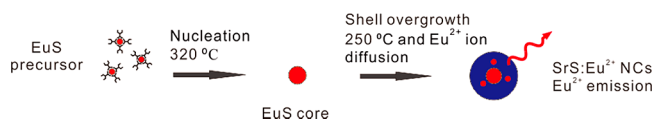


Figure 9. Schematic illustration of the synthesis of SrS:Eu²⁺ NCs using single-source precursors and the nucleation doping strategy.

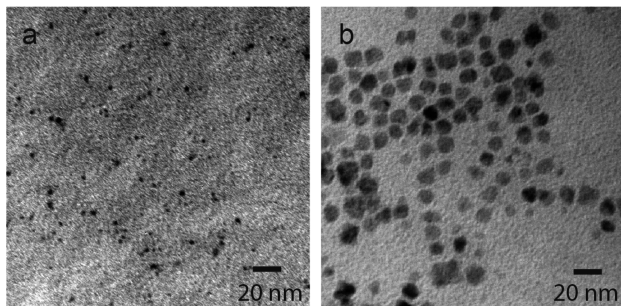


Figure 10. TEM images of NC samples taken from the synthesis of SrS:Eu²⁺ NCs through the nucleation doping strategy: (a) EuS core NCs; (b) EuS/SrS core/shell NCs after SrS shell growth.

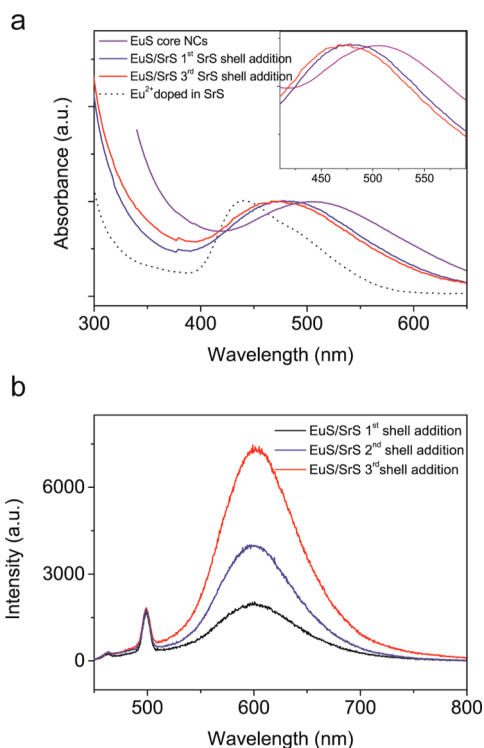


Figure 11. (a) Absorption spectra of SrS:Eu²⁺ NC samples taken during synthesis through the nucleation doping method. The inset shows a magnification of the peak area. (b) Emission spectra of SrS:Eu²⁺ NCs. The samples were excited at 430 nm. The peaks at around 490 nm are due to Raman scattering.

synthesis of the EuS core to achieve small particle sizes. Decomposition of Eu(BDTC)₄ leads to larger core sizes and wider size distribution (Supporting Information, Figure S8). Subsequently, in the same reaction volume, the synthesized EuS NCs were used as “seeds” for heterogeneous nucleation and growth of a SrS shell through slow addition of the Sr(DPTC)₂ precursor at 250 °C. The final EuS/SrS core/shell NCs have sizes ranging from 12 to 20 nm (Figure 10b). Figure 11 presents absorption and emission spectra of purified NC

samples isolated during the SrS shell growth over the EuS cores. We find that the lowest energy absorption peak shifts from 504 to 480 nm upon addition of SrS precursors. This blue shift continues with the thickening of the SrS shell. This indicates that a significant fraction of the Eu²⁺ ions have diffused into the SrS shell, leading to a shift of the 4f⁷ → 4f⁶5d¹ absorption peak of EuS at 504 nm toward the position where Eu²⁺ absorbs when doped into SrS (Figure 7a). Correspondingly, an emission band at 610 nm (Figure 11b), characteristic for SrS:Eu²⁺, appears and becomes stronger upon further shell growth, while the EuS core NC is nonfluorescent.

The results presented above show that the nucleation doping strategy not only is an alternative way to achieve doping but is also complementary to the growth doping strategy. We have shown that the growth doping strategy works best for a combination of dopant and lattice SSPs with similar decomposition temperatures. The nucleation doping method, on the other hand, can be used with combinations of SSPs strongly differing in decomposition temperature, since the decomposition of dopant and lattice SSPs can be performed separately. This flexibility in design of synthesis strategies allows the SSP approach to be applied with a broader range of precursor types.

Although only Eu²⁺ and Ce³⁺ doping has been discussed in this report, the SSP approach for doping developed here and the relation between doping efficiency and reactivity of precursors are expected to be universal. This method has the potential to be widely applicable to the doping of other types of ions, including lanthanides and transition metals, into nanocrystals.

CONCLUSIONS

Through a single-source precursor approach, we have successfully synthesized monodisperse and colloidally stable Ce³⁺- and Eu²⁺-doped SrS and CaS luminescent NCs with diameters of ~10 nm. The luminescence properties of Ce³⁺ and Eu²⁺ in the nanocrystalline host are similar to those of the bulk analogues. The absorption and emission bands are due to f–d transitions which are sensitive to the local coordination of the Ce³⁺ or Eu²⁺ ion. We have used the dopant absorption spectra as probes to semiquantitatively evaluate the doping level. The results reveal that NC doping is kinetically controlled and the doping efficiency is related to the balance of dopant and lattice precursors reactivity. When the chemical structure of the dopant precursors is varied and hence their reactivity is tuned, the doping efficiency can be improved. Moreover, the SSP approach for doping allows for a flexible design of synthesis strategies, as we show with a comparison of growth doping and nucleation doping methods. The successful synthesis of Ce³⁺- and Eu²⁺-doped SrS and CaS luminescent NCs is promising for application as Cd-free luminescent probes. Furthermore, we envision that the SSP doping methods reported here will be widely applicable to the successful doping of other chalcogenide colloidal NCs with luminescent and magnetic dopants.

EXPERIMENTAL SECTION

Preparation of Single-Source Precursors. Calcium diisopropylthiocarbamate, Ca(DPTC)₂, was prepared following the procedures reported by Purdy and George.⁵⁶ A similar method was applied for the synthesis of strontium diisopropylthiocarbamate, Sr(DPTC)₂.³⁷ The dopant precursor europium diethylthiocarbamate diethylammonium salt, Eu(DDTC)₄, was prepared according to the literature.⁵⁷

Cerium diethyldithiocarbamate diethylammonium salt, Ce(DDTC)₄, was prepared under an N₂ atmosphere. A 10 mL portion of a 0.1 M Ce(NO₃)₃·6H₂O (99.99%, Aldrich) solution in anhydrous 2-propanol was mixed with 10 mL of a 0.3 M solution of diethylammonium diethyldithiolcarbamate (98%, Alfa) in 2-propanol. A bright yellow crystalline precipitate was obtained and isolated by centrifugation. The powder obtained was washed with anhydrous 2-propanol, dried under vacuum, and stored under N₂ to prevent oxidation. IR (ATR, cm⁻¹): ν_{C-H}(stretch) 2927 (w), ν_{C-N}(bend) 1469 (s), ν_{C-S}(bend) 996 (s).

Europium butyldithiocarbamate butylammonium salt, Eu(BDTC)₄, was synthesized as follows. Under an N₂ atmosphere, *n*-butylamine (≥99%, Aldrich, 1 mL, 10 mmol) and carbon disulfide (≥99.9%, Aldrich, 0.3 mL, 5 mmol) were added to 5 mL of anhydrous 2-propanol, and the mixture was stirred under N₂ for 10 min. Then, 0.32 g of anhydrous europium(III) chloride (99.9%, Strem Chemicals, 1.25 mmol) dissolved in 5 mL of anhydrous 2-propanol was added dropwise. The initially colorless solution turned orange-red and eventually produced an orange-red precipitate, which was collected through centrifugation, washed with anhydrous 2-propanol, and dried under vacuum. IR (ATR, cm⁻¹): ν_{N-H}(stretch) 3318, 3240, 3175 (m), ν_{C-H}(stretch) 2927 (m), ν_{N-H}(bend) 1505 (s), ν_{C-N}(bend) 1461 (s), ν_{C-H}(bend) 1302 (s), ν_{C-S}(bend) 996 (m).

Europium octyldithiocarbamate octylammonium salt, Eu(ODTC)₄, and europium dodecyldithiocarbamate dodecylammonium salt, Eu(DoDTC)₄, were synthesized using the same method as Eu(BDTC)₄, but using octylamine (99%, Aldrich) and dodecylamine (98%, Aldrich) instead of *n*-butylamine, respectively. IR (ATR, cm⁻¹): Eu(ODTC)₄, ν_{N-H}(stretch) 3318, 3240, 3175 (m), ν_{C-H}(stretch) 2923 (s), ν_{N-H}(bend) 1510 (s), ν_{C-N}(bend) 1461 (s), ν_{C-H}(bend) 1298 (s), ν_{C-S}(bend) 996 (m); Eu(DoDTC)₄, ν_{N-H}(stretch) 3318, 3240, 3175 (w), ν_{C-H}(stretch) 2919 (s), ν_{N-H}(bend) 1510 (s), ν_{C-N}(bend) 1461 (s), ν_{C-H}(bend) 1298 (s), ν_{C-S}(bend) 996 (m).

Cerium butyldithiocarbamate butylammonium salt, Ce(BDTC)₄, and cerium octyldithiocarbamate octylammonium salt, Ce(ODTC)₄, were synthesized using the same method as for their europium counterparts but using Ce(NO₃)₃ instead of EuCl₂. The IR spectra are similar to those of their europium counterparts.

Determination of the Amine-Assisted Decomposition Temperature of Precursors. The amine-assisted decomposition temperatures of dopant SSPs were determined by observing the change in the solution color with heating in oleylamine. Since Ca(DPTC)₂ and Sr(DPTC)₂ do not change color while decomposing in oleylamine, their decomposition temperatures were determined by leading the generated H₂S gas into an aqueous solution of lead acetate and observing the precipitation of black PbS.

Synthesis of Ce³⁺-Doped SrS and CaS NCs through the Growth Doping Method. The syntheses were carried out in a nitrogen-filled glovebox. Oleylamine (70%, Aldrich) was dried under vacuum at 180 °C for 3 h before use to remove moisture and oxygen. For a typical synthesis, a 0.1 M (0.2 M for larger or 0.025 M for smaller particle sizes) solution of Sr(DPTC)₂ (Ca(DPTC)₂ for CaS synthesis) in oleylamine and a solution of Ce(DDTC)₄ in oleylamine (variable concentration) were freshly prepared before use. Then 2 mL of Sr(DPTC)₂ and 1 mL Ce(DDTC)₄ precursor solution were mixed and quickly injected into a three-necked round-bottom flask containing 6 mL of oleylamine at 250 °C. After the injection, the temperature dropped to about 220 °C and was brought back to 250 °C. At this temperature, an Sr shell was grown by the addition of 1 mL of a 0.05 M solution of Sr(DPTC)₂ in oleylamine at a rate of 0.2 mL/min. During the shell growth, the solution turned from light yellow to deep yellow. Subsequently, the reaction temperature was increased to 270 °C for 1 h. Aliquots were taken at different steps of the reaction. The as-synthesized SrS or CaS NCs are capped by oleylamine, which does not provide sufficient colloidal stability at temperatures below 120 °C, leading to partial NC aggregation and turbidity. Therefore, the aliquots and the final product were taken out at temperatures above 120 °C and immediately added to 10 mL of a solution containing 0.6 mL of oleic acid and 20 mg of tetradecylphosphonic acid (TDPA, 97% Aldrich) in toluene. After

recapping with oleic acid and TDPA, which binds more strongly to the SrS or CaS surface, the NCs were washed several times by precipitation with methanol followed by centrifugation. The nanoparticles can be redispersed in common nonpolar solvents, such as toluene and hexane, yielding optically transparent and stable dispersions.

Synthesis of Eu²⁺-Doped SrS and CaS NCs through the Growth Doping Method. The method used to synthesize Eu²⁺-doped SrS (or CaS) NCs was similar to that used for Ce-doped SrS (CaS) NCs, using Eu(BDTC)₄ as the dopant precursor. The only difference is that the shell growth and annealing temperatures were decreased to 200 °C. The annealing was carried out for 15 min.

Synthesis of Eu²⁺-Doped SrS NCs through the Nucleation Doping Method. First, EuS cores were synthesized by injecting 1 mL of freshly prepared 0.05 M Eu(DDTC)₄ solution in oleylamine into a three-necked round-bottom flask containing 6 mL of oleylamine at 320 °C. The reaction solution turned purple immediately after injection. The subsequent growth of a SrS shell was performed in the same reaction flask at 250 °C by slowly adding 2 mL of 0.1 M Sr(DPTC)₂ in oleylamine. Aliquots were taken at different steps of the reaction for analysis. The NCs were recapped and washed using the same procedure described above for the growth doping method.

Characterization of NCs. For optical measurements, washed NCs were redispersed in hexane and loaded in quartz cuvettes sealed under a nitrogen atmosphere. Absorption spectra were recorded on a PerkinElmer Lambda 950 UV/vis/IR spectrophotometer. Emission and excitation spectra were measured on Edinburgh Instruments FLS920 spectrofluorometer equipped with a 450 W Xe lamp with a double monochromator for excitation (gratings blazed at 300 nm (exc) or 500 nm (em)). The emitted light was detected with a Hamamatsu R928 PMT detector. The spectra were corrected for the instrument response. Photoluminescence decay curves were measured by using a PicoQuant time-correlated single-photon counting setup, using either a picosecond 277 nm UV diode or a picosecond 455 nm diode laser. The emission was collected through an optical fiber and dispersed by a 0.1 m monochromator (1350 lines/mm blazed at 500 nm). A fast Hamamatsu photomultiplier tube (H5738P-01) and a Time Harp 200 time-correlated photon counting card were used to record the luminescence decay curves. Absolute quantum yields of NC samples dispersed in hexane were measured on a spectrofluorometer mounted with an integrating sphere.

Elemental analysis of doped NC samples was carried out by inductively coupled plasma atomic emission spectroscopy (ICP-AES). NC samples were washed to remove unreacted precursors, and solvents were evaporated under vacuum. The dry NCs were then dissolved in a mixture of nitric and hydrochloric acid, after which the relative concentrations of different elements were quantified. TEM imaging and electron diffraction measurements were performed on a Tecnai 20F (FEI) microscope. The size distribution of the nanocrystals was estimated through statistical analysis on the TEM images. For each sample, over 100 particles per sample from multiple images were analyzed.

■ ASSOCIATED CONTENT

📄 Supporting Information

Figures and a table giving TEM images, XRD patterns, reference luminescence spectra of bulk material, IR, ICP-AES analysis, and luminescence decay curves. This material is available free of charge via the Internet at <http://pubs.acs.org>.

■ AUTHOR INFORMATION

Corresponding Author

*E-mail for A.M.: a.meijerink@uu.nl

Present Address

^{||}Translational and Molecular Imaging Institute, Icahn School of Medicine at Mount Sinai, New York, NY 10029, USA.

Notes

The authors declare no competing financial interest.

■ ACKNOWLEDGMENTS

The authors thank the Dutch Science Foundation (NWO), the division of Chemical Sciences (C.A.v.W.), for financial support: grant number ECHO.06.B.047. We also acknowledge support from the Debye Institute for the temporary Debye Chair of D.R.G. D.R.G. gratefully acknowledges financial support from the NSF, DMR-1206221. Mr. Gang Wang, MSc is gratefully acknowledged for recording XRD patterns.

■ REFERENCES

- (1) Norris, D. J.; Efros, A. L.; Erwin, S. C. *Science* **2008**, *319*, 1776.
- (2) Wang, F.; Liu, X. *Chem. Soc. Rev.* **2009**, *38*, 976.
- (3) Beaulac, R.; Ochsenbein, S. T.; Gamelin, D. R. In *Nanocrystal Quantum Dots*, 2nd ed.; Klimov, V. I., Ed.; CRC Press: London, 2010; p 397.
- (4) Beaulac, R. M.; Archer, P. I.; van Rijssel, J.; Meijerink, A.; Gamelin, D. R. *Nano Lett.* **2008**, *8*, 2949.
- (5) Sahu, A.; Kang, M. S.; Kompch, A.; Notthoff, C.; Wills, A. W.; Deng, D.; Winterer, M.; Frisbie, C. D.; Norris, D. J. *Nano Lett.* **2012**, *12*, 2587.
- (6) Pradhan, N.; Peng, X. *J. Am. Chem. Soc.* **2007**, *129*, 3339.
- (7) Suyver, J. F.; Wuister, S. F.; Kelly, J. J.; Meijerink, A. *Phys. Chem. Chem. Phys.* **2000**, *2*, 5445.
- (8) Wang, G.; Peng, Q.; Li, Y. *Acc. Chem. Res.* **2011**, *44*, 322.
- (9) Stouwdam, J. W.; van Veggel, F. C. J. M. *ChemPhysChem* **2004**, *5*, 743.
- (10) Smet, P. F.; Moreels, I.; Hens, Z.; Poelman, D. *Materials* **2010**, *3*, 2834.
- (11) Zhao, Y.; Riemersma, C.; Pietra, F.; Koole, R.; de Mello Donegá, C.; Meijerink, A. *ACS Nano* **2012**, *9*, 9058.
- (12) Jia, D. D.; Zhu, J.; Wu, B. Q. *J. Electrochem. Soc.* **2000**, *147*, 386.
- (13) Tamura, Y.; Shibukawa, A. *Jpn. J. Appl. Phys. 1* **1993**, *32*, 3187.
- (14) le Masne de Chermont, Q.; Chaneac, C.; Seguin, J.; Pelle, F.; Maitrejean, S.; Jolivet, J. P.; Gourier, D.; Bessodes, M.; Scherman, D. *Proc. Natl. Acad. Sci. U.S.A.* **2007**, *104*, 9266.
- (15) Krumer, Z.; Pera, S. J.; van Dijk-Moes, R. J. A.; Zhao, Y.; de Brouwer, A. F. P.; Groeneveld, E.; van Sark, W. G. J. H. M.; Schropp, R. E. I.; de Mello Donegá, C. *Sol. Energy Mater. Sol. Cells* **2013**, *111*, 57.
- (16) Erickson, C. S.; Bradshaw, L. R.; McDowall, S.; Gilbertson, J. D.; Gamelin, D. R.; Patrick, D. L. *ACS Nano* **2014**, *8*, 3461.
- (17) Bol, A. A.; van Beek, R.; Meijerink, A. *Chem. Mater.* **2002**, *14*, 1121.
- (18) Buonsanti, R.; Milliron, D. J. *Chem. Mater.* **2013**, *25*, 1305.
- (19) Sun, B. Q.; Yi, G. S.; Chen, D. P.; Zhou, Y. X.; Cheng, J. J. *Mater. Chem.* **2002**, *12*, 1194.
- (20) Kumar, V.; Mishra, V.; Biggs, M. M.; Nagpure, I. M.; Ntwaeaborwa, O. M.; Terblans, J. J.; Swart, H. C. *Appl. Surf. Sci.* **2010**, *256*, 1720.
- (21) Martín-Rodríguez, R.; Geitenbeek, R.; Meijerink, A. *J. Am. Chem. Soc.* **2013**, *135*, 13668.
- (22) Vlaskin, V. A.; Barrows, C. J.; Erickson, C. S.; Gamelin, D. R. *J. Am. Chem. Soc.* **2013**, *135*, 14380.
- (23) Brennan, J. G.; Siegrist, T.; Carroll, P. J.; Stuczynski, S. M.; Brus, L. E.; Steigerwald, M. L. *J. Am. Chem. Soc.* **1989**, *111*, 4141.
- (24) Pradhan, N.; Efrima, S. *J. Am. Chem. Soc.* **2003**, *125*, 2050.
- (25) Pradhan, N.; Katz, B.; Efrima, S. *J. Phys. Chem. B* **2003**, *107*, 13843.
- (26) Trindade, T.; O'Brien, P. *J. Mater. Chem.* **1996**, *6*, 343.
- (27) Hanif, K. M.; Meulenbergh, R. W.; Strouse, G. F. *J. Am. Chem. Soc.* **2002**, *124*, 11495.
- (28) Archer, P. I.; Santangelo, S. A.; Gamelin, D. R. *Nano Lett.* **2007**, *7*, 1037.
- (29) Archer, P. I.; Santangelo, S. A.; Gamelin, D. R. *J. Am. Chem. Soc.* **2007**, *129*, 9808.
- (30) Mukherjee, P.; Shade, C. M.; Yingling, A. M.; Lamont, D. N.; Waldeck, D. H.; Petoud, S. P. *J. Phys. Chem. A* **2010**, *115*, 4031.
- (31) Saha Chowdhury, P.; Patra, A. *Phys. Chem. Chem. Phys.* **2006**, *8*, 1329.
- (32) Sarkar, S.; Karan, N. S.; Pradhan, N. *Angew. Chem., Int. Ed.* **2011**, *50*, 6065.
- (33) Malik, M. A.; Afzaal, M.; O'Brien, P. *Chem. Rev.* **2010**, *110*, 4417.
- (34) Radovanovic, P. V.; Gamelin, D. R. *J. Am. Chem. Soc.* **2001**, *123*, 12207.
- (35) Pradhan, N.; Goorskey, D.; Thessing, J.; Peng, X. *J. Am. Chem. Soc.* **2005**, *127*, 17586.
- (36) Chen, D.; Viswanatha, R.; Ong, G. L.; Xie, R.; Balasubramanian, M.; Peng, X. *J. Am. Chem. Soc.* **2009**, *131*, 9333.
- (37) Zhao, Y.; Rabouw, F. T.; Donegá, C. d. M.; Meijerink, A.; van Walree, C. A. *Mater. Lett.* **2012**, *80*, 75.
- (38) Jung, Y. K.; Kim, J. I.; Lee, J. K. *J. Am. Chem. Soc.* **2009**, *132*, 178.
- (39) Yang, Y.; Chen, O.; Angerhofer, A.; Cao, Y. C. *J. Am. Chem. Soc.* **2008**, *130*, 15649.
- (40) Jia, D.; Wang, X.-j. *Opt. Mater.* **2007**, *30*, 375.
- (41) Huttl, B.; Troppenz, U.; Velthaus, K. O.; Ronda, C. R.; Mauch, R. H. *J. Appl. Phys.* **1995**, *78*, 7282.
- (42) Okamoto, F.; Kato, K. *J. Electrochem. Soc.* **1983**, *130*, 432.
- (43) Bachmann, V.; Ronda, C.; Meijerink, A. *Chem. Mater.* **2009**, *21*, 2077.
- (44) Pan, Y.; Wu, M.; Su, Q. *J. Phys. Chem. Solids* **2004**, *65*, 845.
- (45) Ravotti, F.; Benoit, D.; Lefebvre, P.; Valvin, P.; Vaille, J. R.; Dusseau, L.; Fesquet, J.; Gasiot, J. *J. Appl. Phys.* **2007**, *102*, 123102.
- (46) Meltzer, R. S.; Feofilov, S. P.; Tissue, B.; Yuan, H. B. *Phys. Rev. B* **1999**, *60*, R14012.
- (47) Rabouw, F. T.; den Hartog, S. A.; Senden, T.; Meijerink, A. *Nat. Commun.* **2014**, *5*, 3610.
- (48) Brokmann, X.; Coolen, L.; Dahan, M.; Hermier, J. P. *Phys. Rev. Lett.* **2004**, *93*, 107403.
- (49) Lunnemann, P.; Rabouw, F. T.; van Dijk-Moes, R. J. A.; Pietra, F.; Vanmaekelbergh, D.; Koenderink, A. F. *ACS Nano* **2013**, *7*, 5984.
- (50) Mirkovic, T.; Hines, M. A.; Nair, P. S.; Scholes, G. D. *Chem. Mater.* **2005**, *17*, 3451.
- (51) Akhtar, J.; Malik, M. A.; O'Brien, P.; Helliwell, M. J. *Mater. Chem.* **2010**, *20*, 6116.
- (52) Gupta, S.; Kershaw, S. W.; Rogach, A. L. *Adv. Mater.* **2013**, *25*, 6923.
- (53) Van Haecke, J. E.; Smet, P. F.; De Keyser, K.; Poelman, D. *J. Electrochem. Soc.* **2007**, *154*, J278.
- (54) Shannon, R. *Acta Cryst. A* **1976**, *32*, 751.
- (55) Huxter, V. M.; Mirkovic, T.; Nair, P. S.; Scholes, G. D. *Adv. Mater.* **2008**, *20*, 2439.
- (56) Purdy, A. P.; George, C. F. *Main Group Chem.* **1996**, *1*, 229.
- (57) Regulacio, M. D.; Kar, S.; Zuniga, E.; Wang, G.; Dollahon, N. R.; Yee, G. T.; Stoll, S. L. *Chem. Mater.* **2008**, *20*, 3368.